Engineering Geology 186 (2015) 68–78

Contents lists available at ScienceDirect

Engineering Geology

journal homepage: www.elsevier.com/locate/enggeo

Landslide dam deformation analysis under aftershocks using large-scale shaking table tests measured by videogrammetric technique

Zhen-Ming Shi [a,b,d], You-Quan Wang [a,b,c], Ming Peng [a,b,*], Sheng-Gong Guan [a,b], Jian-Feng Chen [a,b]

[a] Key Laboratory of Geotechnical and Underground Engineering of Ministry of Education, Tongji University, Shanghai 200092, China
[b] Department of Geotechnical Engineering, College of Civil Engineering, Tongji University, Shanghai 200092, China
[c] Shanghai Geotechnical Investigations & Design Institute Co., Ltd., Shanghai 200438, China
[d] Collaborative Innovation Center of Geohazard Prevention (CICGP), Chengdu, Sichuan 610059, China

ARTICLE INFO

Article history:
Accepted 18 September 2014
Available online 30 September 2014

Keywords:
Landslide dam
Shaking table test
Dam deformation
Videogrammetric technique
Aftershock

ABSTRACT

The Ms 8.0 Wenchuan earthquake triggered at least 257 landslide dams. More than 849 aftershocks with magnitudes higher than Ms 4.0 occurred after the Wenchuan earthquake by 12 March, 2012 (Shen et al., 2013), which might largely influence the structure and soil properties of these dams. This paper aims to study the dynamic deformation of landslide dams under aftershocks through larger scale shaking table tests. Videogrammetric technique was applied to measure the dynamic deformation of the model dams. Two groups of shaking table tests were conducted with two types of landslide dam materials: one with quartz sands containing 10% kaolin (Dam I) and the other with only quartz sands (Dam II). The dam deformation and its influencing factors were analyzed with the results measured by videogrammetric technique. The deformations were generally higher on the surface of the dams, either on the crest or on the both upstream and downstream slopes. Higher peak ground acceleration (PGA) resulted in larger dam deformations due to higher seismic force. The deformations under the combination of *X*- and *Z*-directional shakings were larger than those under *X*-directional shaking for sufficient vibratory compaction. Water rising led to the increase of dam deformations because that the water seepage reduced the effective soil stress, especially reduced the matric suction. The settlements of the dam composed of more fine particles were larger than that composed of large particle size because that the soil pores in the former were filled more sufficiently with fine particles. The aftershocks may not directly trigger the failures of landslide dams, but accelerate the overtopping failures by lowering the dam crest with settlement and cracking.

1. Introduction

Floods from dam/levee break pose huge risks to the people and properties downstreams (Courage et al., 2013; Jongejan and Calle, 2013; Zhang et al., 2013). The Ms 8.0 Wenchuan earthquake triggered at least 257 landslide dams (Cui et al, 2009). More than 849 aftershocks with magnitudes higher than Ms 4.0 occurred after the Wenchuan earthquake by 12 March, 2012 (Shen et al., 2013). There are numbers of studies on the static behaviors of landslide dams, for instance, stability analysis, failure modes, and breach parameters (e.g., Costa and Schuster, 1988, 1991; Korup, 2002; Ermini and Casagli, 2003; Davies et al., 2007; Shi et al., 2011; Peng and Zhang, 2012). However, the researches on dynamic behaviors of landslide dams are seldom found. Shaking table tests were conducted in the paper for this purpose.

In shaking table tests, the acceleration and displacement were normally measured by traditional acceleration sensors and displacement gauges. It would become very inefficient if detailed measurements of many points are needed. Moreover, the installing of traditional sensors may largely change the soil mechanics properties of the landslide dams, which may result in large systematic measurement errors. Videogrammetric technique was used to solve the problems addressed above in this paper.

Videogrammetric technique, also called digital close-range photogrammetry, is an advanced version of photogrammetry, which combined the photogrammetric technique and computer vision. Digital images of video sequences of objects are acquired by cameras with photogrammetric technique. Computer vision provides theoretical supports and basic algorithmic for videogrammetric techniques and enables computers to understand and interpret visual information from the images (Gruen, 1997; Ji, 2007). Videogrammetric technique does not change the soil properties during testing, since it is a non-contact measurement technology. A great number of particles can be measured and tracked simultaneously with high accuracy with the method.

* Corresponding author at: Key Laboratory of Geotechnical and Underground Engineering of Ministry of Education, Tongji University, Shanghai 200092, China.
E-mail address: pengming@tongji.edu.cn (M. Peng).

http://dx.doi.org/10.1016/j.enggeo.2014.09.008
0013-7952/

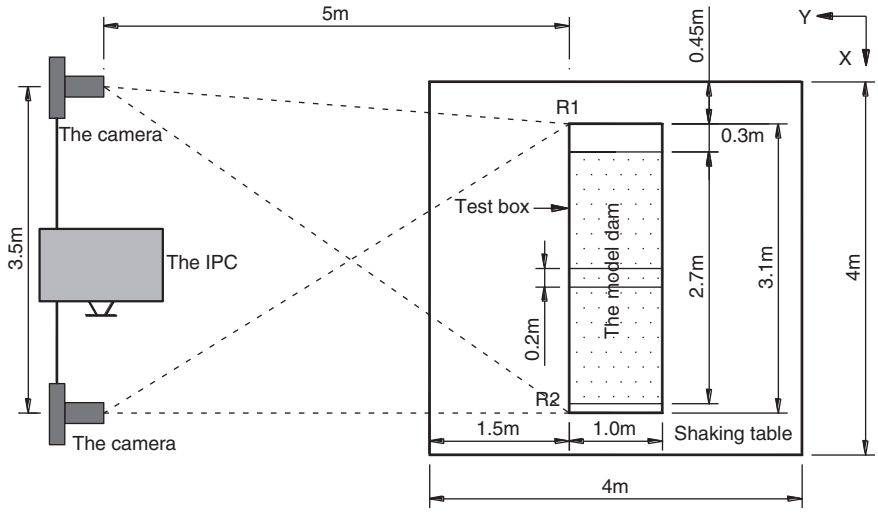

Fig. 1. The layout of the test equipment.

Videogrammetric technique has been applied in the Aeronautics and Astronautics, automobile collision tests, railway track measurement, etc. (Burner and Liu, 2001; Ji, 2007; Yu et al., 2008). In civil engineering, videogrammetric technique has been applied in architectural structures, bridges, etc. (Fu et al., 2002; Chang and Ji, 2007; Chang and Xiao, 2010; Ye et al., 2011). The applications of videogrammetric technique in geotechnical engineering were also reported (e.g., Robson et al., 1998; Taylor et al., 1998; Paikowsky and Xi, 2000; Cleveland and Wartman, 2006). In this study, high speed videogrammetric technique is applied to measure the accelerations and dynamic deformation of landslide dams.

This paper aims to study the dynamic deformation and the corresponding influences factors of landslide dams under aftershocks through larger-scale shaking table tests. Videogrammetric technique was used to measure the deformation and acceleration of model dams. First, the shaking table tests of landslide dams and the layout of the equipments were illustrated. Then, the measurement methods and principle of the videogrammetric technique were introduced, the precision and reliability of which was validated. Finally, the landslide dam deformation under seismic action was analyzed as well as the influence factors.

2. The large-scale shaking table tests of landslide dams with videogrammetric technique

2.1. The layout of the test equipment

The layout of the test equipment is shown in Fig. 1. The equipment mainly includes the shaking table and videogrammetric technique system. The shaking table is a large-scale 3-dimensional shaking table with six degrees of freedom. The platform size is 4 m × 4 m and the maximum load capacity is 25 tons. The working frequency ranges from 0.1 to 50 Hz. The maximum driving displacement and driving speed are ±100 mm and 1000 mm/s in *X* direction (horizontal) and ±50 mm and 600 mm/s in *Y* (horizontal) or *Z* (vertical) direction, respectively. The maximum driving acceleration in *X*, *Y* and *Z* directions are 1.2 g, 0.8 g and 0.7 g.

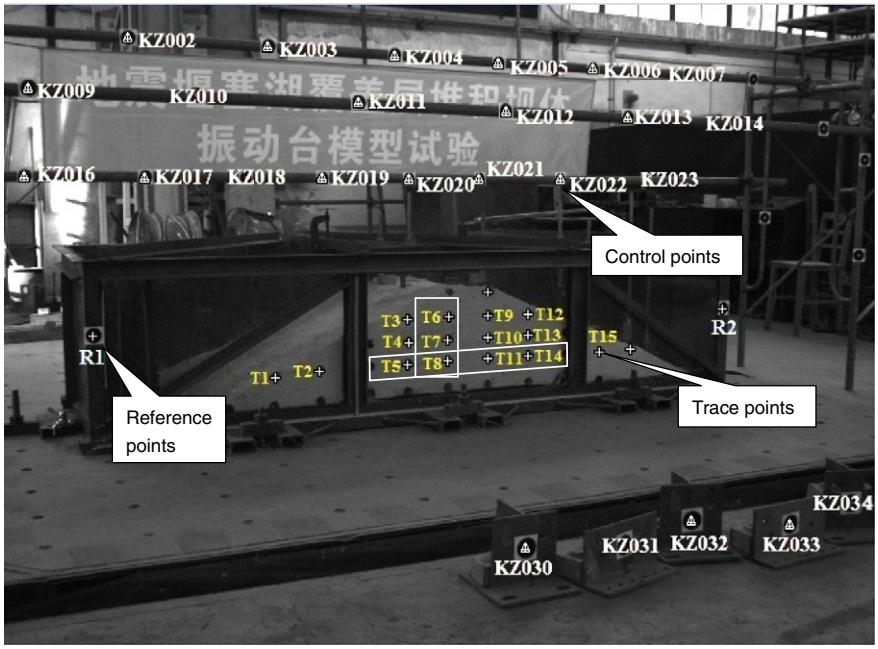

Fig. 2. Layout of the circle labels in Dam I.

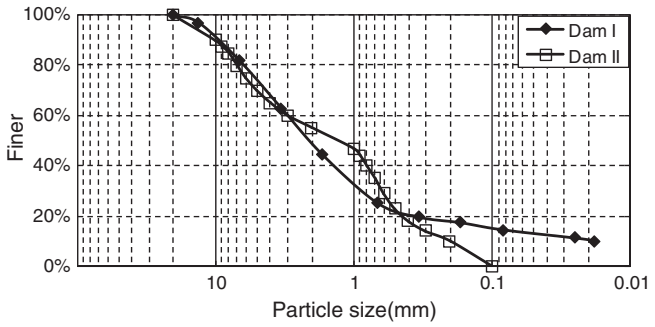

Fig. 3. Particle size distribution curves of model dam materials.

Table 1
Similarity law of the shaking table tests (based on Iai, 1988; Liu et al., 2005).

Parameter	Relationship	Similarity coefficient
Length (L)	C_l	20
Density of the dam (ρ)	C_ρ	1
Density of water (ρ_f)	$C_{\rho_f} = C_\rho$	1
Acceleration (g)	$C_a = C_g = 1$	1
Modulus coefficient (C)	$C_c = C_p/C_m$	4
Stress (σ)	$C_\sigma = C_\rho C_l$	20
Strain (ε)	$C_\varepsilon = C_\rho^{1/2} C_l^{1/2}/C_c$	1.118
Displacement (u)	$C_u = C_\rho^{1/2} C_l^{3/2}/C_c$	22.36
Damping ratio (ξ)	$C_\xi = 1$	1
Time (t)	$C_t = {C_\rho}^{1/4} {C_l}^{3/4}/{C_c}^{1/2}$	4.729
Frequency (f)	$C_f = {C_\rho}^{-1/4} {C_l}^{-3/4} {C_c}^{1/2}$	0.211 (or 1/4.729)

The videogrammetric technique system in the tests included two high-speed cameras, lens, an industrial personal computer (IPC), and circle labels. Two Falcon 4M60 high-speed cameras were used in the tests. The resolution of the camera was 2352 (H) by 1728 (V) pixels. The lens of the cameras had the focus of 20 mm. The frame frequency was set as 60 frames per second (fps). The distance between the two cameras was 3.5 m. The distance of the cameras from the test box is 5 m, as shown in Fig. 1. The cameras were linked to the IPC, which can take and process the photos automatically.

The circle labels included 25 control points (with 2 invalid points) and more than 15 trace points, as shown in Fig. 2. The control points were pasted on the steel beams above the test box and the steel blocks in front of the box, which were fixed to the ground. The trace points were buried in the dam, which could be observed by the cameras through a glass wall. Two reference points (R1 and R2) were pasted on the test box to get the relative displacement between the dam and the test box. The coordinates of control points and reference points were measured by the electronic total station before the shaking tests.

2.2. Design of the model dams

Two groups of tests were conducted to simulate the dynamic behaviors of two types of landslide dams: one (Dam I) with 90% quartz sand and 10% kaolin according to the samples in Donghekou landslide dam caused by the Wenchuan earthquake, China (Xie, 2009; Chang et al., 2011); and the other (Dam II) with quartz sands for comparison. The grading curves of the two dam materials are shown in Fig. 3.

The determination of the similitude for the shaking table tests, which is shown in Table 1, was based on Iai (1988) and Liu et al. (2005). There are four independent scaling factors: the factors of geometry (length), density, acceleration and modulus coefficient. The geometric scaling factor of 1:20 was fixed considering the maximum working frequency of the shaking table (50 Hz); the density scaling factor was set as 1; the scaling factor of acceleration was 1 in the 1 g gravitational field; and the modulus coefficient C is a dimensionless parameter, which is related to the density and particle size distribution of materials. The scaling factor of C was set as 4 referring to the tests of man-made dam materials (Liu et al, 2005). The detailed similitude ratios of other physical parameters are shown in Table 1.

The geometric parameters of these two types of landslide dam models were the same, with a height of 0.5 m, a length of 1.0 m (perpendicular to the river direction), a crest width of 0.2 m and a bottom width of 2.7 m, as shown in Fig. 4. Acceleration sensors were set to capture the seismic accelerations for comparison. The layout of the acceleration sensors and the sketch of the model dams are shown in Fig. 4.

The model dams were constructed with the dry density of 1.78 g/cm^3 according to Donghekou Landslide Dam (Xie, 2009; Chang et al., 2011). The soil properties with the dry density were shown in Table 2. The model dams are constructed with 5 layers totally and with a height of 10 cm in each layer. The studied landslide model dams are different from the man-made model dams for smaller compactness, higher permeability and gentler slope angle. Moreover, the particle sizes of the studied dams were according to the materials of the Donghekou landslide dam (Xie, 2009; Chang et al, 2011).

2.3. Test process

Three types of seismic waves were set in each group of tests: El Centro wave, Kobe wave and Wenchuan wave, with peak accelerations of 0.071 g, 0.2 g, 0.41 g and 0.63 g, respectively. The acceleration time history and Fourier spectra of the seismic wave were illustrated by Shi et al. (2014). The basic characteristic parameters of the seismic waves were shown in Table 3. The tests were carried out in two water stages, with the water depth of 0 and 0.25 m, respectively. The test inputs in Stage 1 are listed in Table 4. The test process is as follows: First, Step 1 with the white noise with the peak acceleration of 0.05 g was carried out to obtain the dynamic properties of landslide dams. And then, Step 2 with X-directional El Centro Wave with the peak acceleration of 0.071 g was carried out to obtain the distribution of acceleration

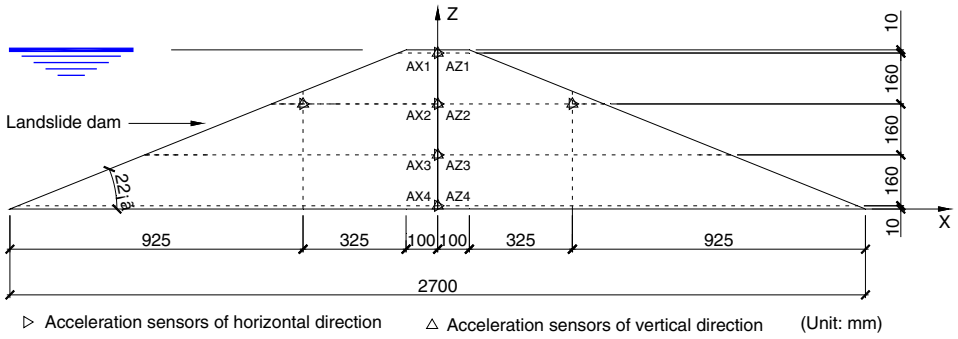

Fig. 4. Layout of the acceleration sensors in the model dams.

Table 2
Physical properties of model dam materials.

Dam materials	Dry density (g/cm^3)	Minimum dry density (g/cm^3)	Maximum dry density (g/cm^3)	Compactness
Dam I	1.78	1.44	2.05	0.642
Dam II	1.78	1.54	1.93	0.667

Table 3
Basic characteristic parameters of the seismic waves.

Seismic wave	Predominant frequency of prototype wave (Hz)	Time of prototype wave (s)	Predominant frequency of model wave (Hz)	Time of model wave (s)
El Centro Wave	1.0–2.2	54	4.7–10.4	11.42
Kobe Wave	1.0–3.0	40	4.7–14.2	8.46
Wenchuan Wave	2.2–6.0	120	10.4–28.4	25.38

amplification factor and the deformation of the model dam using the videogrammetric technique. Steps 3 to 7 were carried out with the inputs in Table 4 successively. Then Step 8 with white noise was carried out to obtain the dynamic properties after the dam was shaken by earthquakes in the test case Steps 2 to 7. The peak acceleration changed to 0.2 g, 0.41 g, 0.63 g to repeat the test process above. The test cases in Stage 2 repeated the earthquake waves, with the water depth of 0.25 m. More details of the tests refer to Shi et al. (2014).

3. Data acquisition and processing with videogrammetric technique

In the tests, two high speed cameras were applied to measure the geometrical parameters through taking photographs. Displacement, velocity and acceleration can be obtained by processing these photographs. The procedure of the videogrammetric technique measurement in the test is shown as follows.

(1) The coordinate system was established by electronic total station with the 15 of the 23 control points before shaking table tests. The rest of 8 control points were used to qualify the precision of videogrammetric technique.
(2) The trace points were observed by taking photos. The coordinates of these trace points were obtained with these photos based on the coordinate system.
(3) The displacement, velocity and acceleration of the trace points were calculated with these coordinates. The details of the method will be introduced as follows.

The sketch of data processing in the shaking table test with videogrammetric technique is shown in Fig. 5. The sketch in full line is the 1st photo, and the sketch in dotted line is the nth photo. R_1 and R_n are the positions of the reference point in the 1st and nth photos, respectively. T_{m1} and T_{mn} are the positions of the mth trace point T_m in the 1st and nth photos, respectively.

The three-dimensional displacement in the nth photograph of the point T_m can be calculated as

$$\mathbf{D_{mn}}=\mathbf{P_{mn}}-\mathbf{P_{m1}} \tag{1}$$

where $\mathbf{D_{mn}} = [DX_{mn}, DY_{mn}, DZ_{mn}]^T$ is the displacement of the monitoring point T_m in the nth photograph in the X, Y and Z directions; $\mathbf{P_{m1}} = [X_{m1}, Y_{m1}, Z_{m1}]^T$ and $\mathbf{P_{mn}} = [X_{mn}, Y_{mn}, Z_{mn}]^T$ are the coordinates of the point in the 1st and nth photographs.

The velocity of T_m in nth photograph is assumed as the average velocity between the nth and $(n + 1)$th photographs, which can be given by

$$\mathbf{V_{mn}}=\left(\mathbf{P_{m(n+1)}}-\mathbf{P_{mn}}\right)/\Delta\mathbf{T} \tag{2}$$

where $\mathbf{V_{mn}} = [VX_{mn}, VY_{mn}, VZ_{mn}]^T$ is the velocity of T_m in the nth photograph in the three directions. ΔT is the time interval between the nth and $(n + 1)$th photograph.

The acceleration of T_m in the nth photograph, $\mathbf{a_{mn}} = [aX_{mn}, aX_{mn}, aX_{mn}]^T$, can be calculated as

$$\mathbf{a_{mn}}=\left(\mathbf{V_{m(n+1)}}-\mathbf{V_{mn}}\right)/\Delta\mathbf{T}. \tag{3}$$

The deformation of the model landslide dam can be treated as the relative displacement of the monitoring point. The relative displacement of the monitoring points T_m in the nth photograph, $\mathbf{\Delta_{mn}} = [\Delta x_{mn}, \Delta y_{mn}, \Delta z_{mn}]^T$ is given by

$$\mathbf{\Delta_{mn}}=\mathbf{P_{mn}}-\mathbf{P_{Rn}}-\mathbf{\Delta_1} \tag{4}$$

where $\mathbf{P_{Rn}} = [X_{Rn}, Y_{Rn}, Z_{Rn}]^T$ is the coordinate of reference point R in the nth photograph. $\mathbf{\Delta_1}$ is the relative displacement between the reference point R and T_m in the first photograph:

$$\mathbf{\Delta}_1 = [X_{m1}-X_{R1}, Y_{m1}-Y_{R1}, Z_{m1}-Z_{R1}]^T. \tag{5}$$

Table 4
Test process of Stage 1 (without water).

Steps	Test case	Peak ground acceleration (g)		Note
		X direction	Z direction	
1	1WN	0.05	0.05	White noise
2, 3, 4	EL1-0, KB1-0, WC1-0	0.071	–	
5, 6, 7	EZ1-0, KZ1-0, WZ1-0	0.071	0.046	
8	2WN	0.05	0.05	White noise
9, 10, 11	EL2-0, KB2-0, WC2-0	0.2	–	
12, 12, 13	EZ2-0, KZ2-0, WZ2-0	0.2	0.13	
15	3WN	0.05	0.05	White noise
16, 17, 18	EL3-0, KB3-0, WC3-0	0.41	–	
19, 20, 21	EZ3-0, KZ3-0, WZ3-0	0.41	0.27	
22	4WN	0.05	0.05	White noise
23, 24, 25	EL4-0, KB4-0, WC4-0	0.63	–	
26, 27, 28	EZ4-0, KZ4-0, WZ4-0	0.63	0.41	
29 (1), 29 (2)	5WN, 6WN	0.05	0.05	White noise

Notes: WC — Wenchuan Wave (X direction); WZ — Wenchuan Wave (X and Z two directions); KB — Kobe Wave (X direction); KZ — Kobe Wave (X and Z two directions); EL — El Centro Wave (X direction); EZ — El Centro Wave (X and Z two directions); X:Z = 1:0.65.

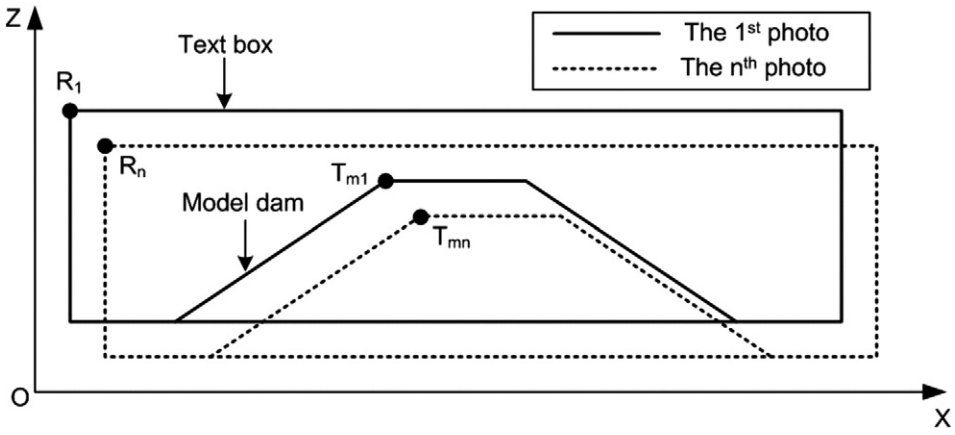

Fig. 5. The sketch of data processing in the shaking table test with videogrammetric technique.

Table 5
Comparison of the coordinates of the 8 check points measured by the electronic total station and the videogrammetric technique.

Point number	Measured by the electronic total station (m)			Measured by the videogrammetric technique (m)			Difference value (mm)		
	X	*Y*	*Z*	*X*	*Y*	*Z*	DX	DY	DZ
KZ005	6.3853	3.6327	5.215	6.3859	3.6325	5.2145	0.6	−0.2	−0.5
KZ010	4.8096	3.1301	4.955	4.8088	3.1313	4.9556	−0.8	1.2	0.6
KZ021	6.5544	4.1448	4.666	6.5553	4.1450	4.6655	0.9	0.2	−0.5
KZ022	7.0736	4.1486	4.672	7.0737	4.1479	4.6712	0.1	−0.7	−0.8
KZ031	5.6333	1.4572	3.608	5.6339	1.4564	3.6082	0.6	−0.8	−0.2
KZ034	6.5099	1.4418	3.62	6.5100	1.4426	3.6199	0.1	−0.8	−0.1
KZ014	7.444	3.1435	4.945	7.4444	3.1444	4.9449	0.4	0.9	−0.1
KZ018	5.2611	4.1398	4.658	5.2616	4.1397	4.6590	0.5	−0.1	−1.0
RMS							0.48	0.72	0.52

4. Precision of the measurement results by the videogrammetric technique

4.1. The precision of the measured positions

Eight of the 25 control points were selected to verify the precision of the videogrammetric technique measurement results. Taking the test Step 24 of Dam I as an example, Kobe Wave with PGA of 0.63 g in *X*-direction was input and the water depth was set as 0 m. Table 5 shows the comparison of the coordinates of the 8 check points measured by the Electronic Total Station and the videogrammetric technique, respectively. The measured results in these two methods were relatively close. The root mean squares (RMS) of *X*, *Y* and *Z* coordinates were 0.48 mm, 0.72 mm and 0.52 mm, respectively, which are all less than 1 mm. Besides, the variations of the measured results in any fixed control point was less than 0.1 mm, which indicated that the cameras were not obviously affected by the shaking table tests or other interruptions.

4.2. The precision of the accelerations

Fig. 6 shows the accelerations of the input seismic wave and the measured accelerations of the reference point R1 on the test box (Figure 2) in the test case Step 24. The two curves coincide well, which indicates relatively good precision of the measurement.

Fig. 7 shows the accelerations of T6 (Figure 2) measured by videogrammetric technique and of AX2 (Figure 4) measured by the acceleration sensor in the test case Step 24. T6 and AX2 were very close, thus the measured accelerations of these two points were applicable to verify the videogrammetric technique measurement. The time history of the accelerations with these two methods was very close, but amplitudes differed in certain degree, as shown in Fig. 7. The reason was that the sampling frequency of the cameras in the tests was 60 Hz. It might be not high enough to obtain the exact accelerations by processing 60 photos in each second, since the predominant frequencies of the input waves were in the range of 4.7–28.4 Hz. It could be solved by using cameras with higher sampling frequency in further study. In this paper, the measured accelerations were not analyzed but the dam deformations. The latter was not obviously influenced by the sampling frequency.

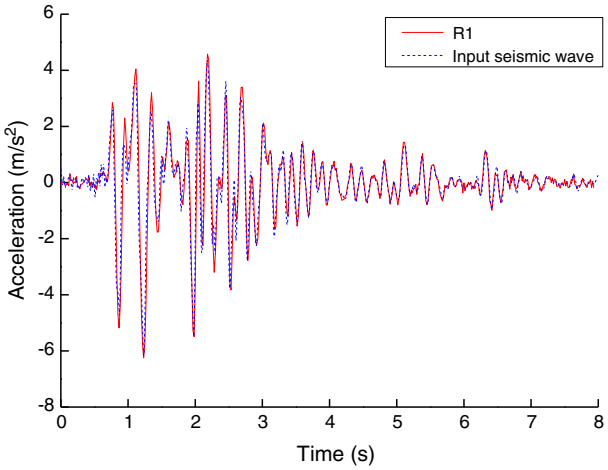

Fig. 6. Comparison of acceleration time history of R1 and the input seismic wave.

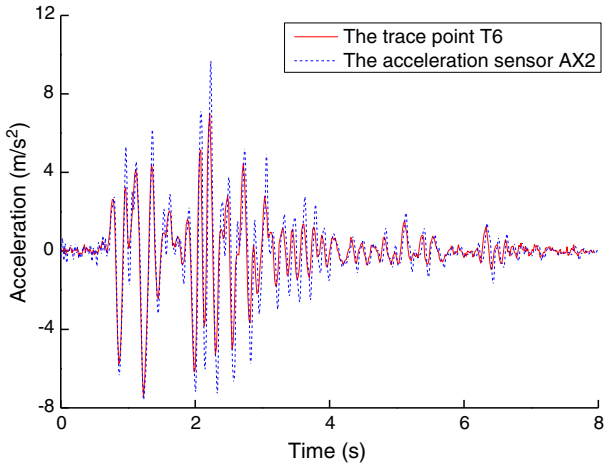

Fig. 7. Comparison of the acceleration time history measured by videogrammetric technique at the trace point T6 and by the acceleration sensor AX2.

Table 6
Typical test cases for dam deformation analysis.

Steps	Test case	Peak ground acceleration (g)		Water depth (m)
		X direction	*Z* direction	
17	KB3-0	0.41	N/A	0
24	KB4-0	0.63	N/A	0
27	KZ4-0	0.63	0.41	0
31	KB1-25	0.071	N/A	0.25
38	KB2-25	0.2	N/A	0.25
45	KB3-25	0.41	N/A	0.25

5. Test results and discussion

5.1. The distribution of the deformation

The dam deformations were measured by the displacement of the trace points. The inputs of some typical test cases are shown in Table 6. Fig. 8 shows the displacement vectors of the trace points in Dam I in test case Step 24. The arrows in the figure indicate the vectors of the deformation with magnitudes and directions. The settlements (*Z*-directional deformation) increased from dam bottom to crest, as also shown in Fig. 9a, with the largest displacement of 2.9 mm in the trace points T6. One reason was that the settlements in the upper layer of soils were the accumulation of the settlements of the soils under it. Another reason might be that the acceleration amplification factors increased from dam bottom to crest, which indicated increasing dynamic forces (Shi et al., 2014). Fig. 10 shows the relationship of *X*-directional acceleration amplification factor β with different peak ground accelerations (PGA) and dam heights, which shows β increased obviously with dam height.

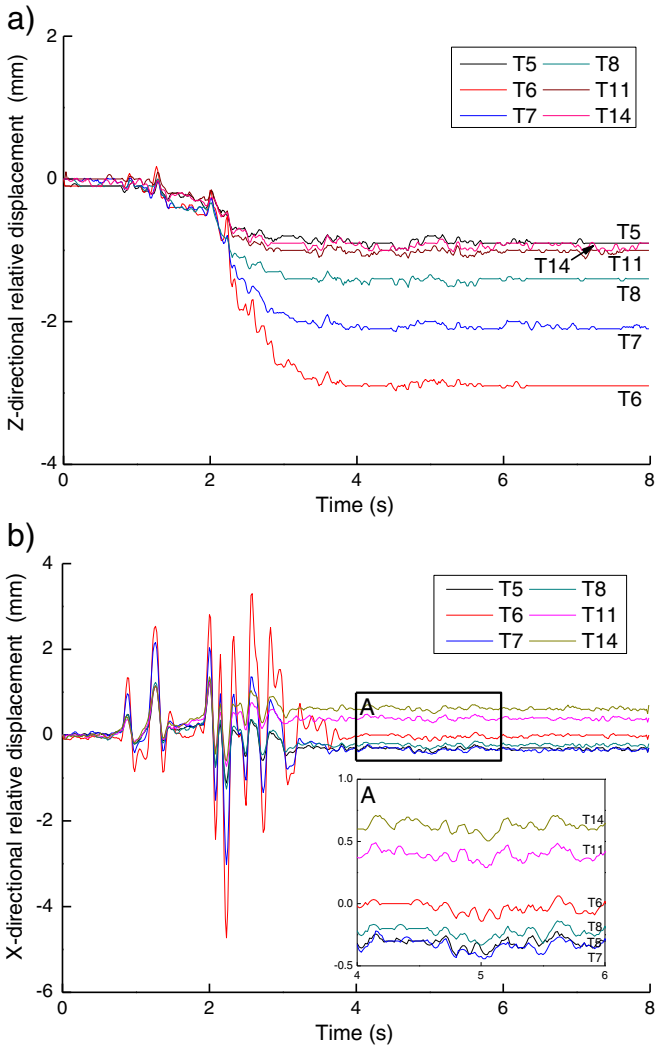

Fig. 9. The displacements of the trace points in the test case Step 24 of Dam I: (a) *Z*-directional; (b) *X*-directional.

The *X*-directional displacements of these trace points are shown in Figs. 8 and 9b. Normally, the trace points with positive *X*-coordinates (the right part) moved downstream and vice versa. Taking the points of T5, T8, T11 and T14 for instance, which located with the same height from upstream to downstream, the *X*-directional displacements of these four points moved from leftward (to upstream) to rightward (to downstream) directions. While, the *X*-directional displacements of the points close to the middle of the dam ($X = 0$) were close to zero.

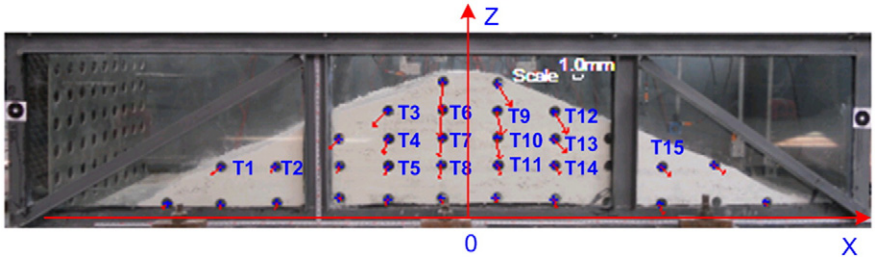

Fig. 8. The dam deformation of Dam I in test case Step 24 (the arrow means the vector of the displacement).

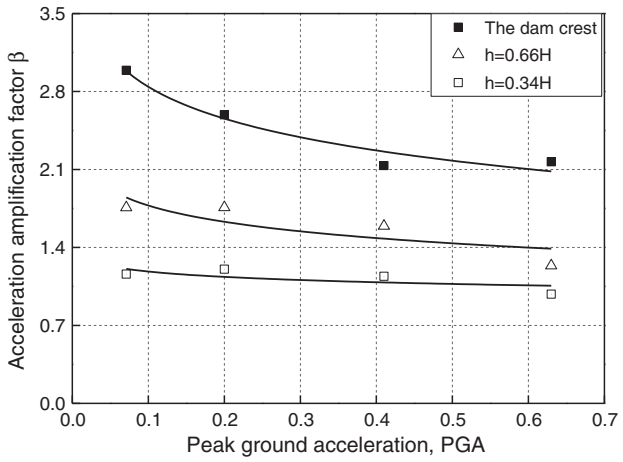

Fig. 10. The relationship of *X*-directional acceleration amplification factor, β, and peak ground acceleration (PGA) under *X*-directional seismic waves.

Table 7
The displacements of the typical trace points in Dam II in Step 24 (*X*-directional wave) and Step 27 (*X*- and *Z*-directional waves).

Displacement direction	Trace points (shown in Figure 11)	Displacements (mm)		Difference (mm)
		In Step 24[a]	In Step 27[a]	
Vertical	A1	0.4	0.8	0.4
	B1	0.3	0.8	0.5
	C1	0.3	0.6	0.3
	D1	0.2	0.4	0.2
	E1	0.3	0.4	0.1
Horizontal	A2	0.1	0.2	0.1
	B4	0.1	0.7	0.6
	C5	0.2	1.1	0.9
	D6	0.1	1.0	0.9
	E7	0.1	0.5	0.4

Note:
[a] The seismic wave and water depth are shown in Table 6.

5.2. Influence factors of dam deformation

5.2.1. Combination of X- and Z-directional seismic waves

The test cases Steps 24 and 27, as shown in Table 4, had the same water depth (0 m) and *X*-directional PGA. The only difference between these two cases was that Step 27 was operated with the combination of *X*- and *Z*-directional seismic waves. Thus, the comparison of these two cases shows the influence of the *Z*-directional seismic wave on dam deformation. Fig. 11 shows the displacement vectors of Dam II in Steps 24 and 27. The displacements under the combination of *X*- and *Z*-directional seismic actions were much larger than those under solo *X*-directional actions. The detailed differences of displacements of some typical trace points in these two cases are shown in Table 7. It can be explained as that the combination of *X*- and *Z*-directional seismic actions compacted the soils more sufficiently. More fine particles could move into the pores of the coarse particles during vibrant compaction.

5.2.2. Peak ground acceleration (PGA)

The test cases of Steps 31, 38 and 45 had PGAs of 0.071, 0.2 and 0.41 g, respectively. As the other sets of these three cases were the same, the results of them showed the influences of PGA on dam displacements. The displacements obviously increased with PGA as shown in Fig. 12. Although the acceleration amplification factor, β, slightly decreased with the increase of PGA (as shown in Figure 10), higher PGA led to larger dynamic forces (proportional to the product of PGA and β), which incurred large displacements. The decrease of β with PGA may be caused by the decrease of shear modulus due to larger dam deformation. Another important reason is that the previous accumulative seismic actions had already resulted in large dam deformation, which led to smaller β. The displacements of the points close to the dam crest and the downstream slope surface had larger increments. The reason may be that these points had less constraint and could move more freely. The detailed horizontal and vertical displacements of some typical trace points are shown in Fig. 13.

5.2.3. Water depth

Water depth was a very sensitive factor to the trace point displacements. The comparison of the cases Step 17 with the water depth of 0 m and Step 45 with the water depth of 0.25 m shows the influence of water depth on dam deformation. As shown in Table 8, the largest vertical displacement increment was 1.9 mm in Trace point A1 and the correspondingly horizontal one was 1.4 mm in Trace point C5. The intuitive vision of the differences in these two cases is shown in Fig. 14. One reason for the large increment by water may be that the increasing of pore water pressure weakened the effective stress of soils, especially reduced the soil matric suction. The structure of the dam with water depth of 0 m was dominated by the matric suction, since it mainly consisted of dry sands. The high suction resulted in strong contact forces among the soil particles, which led to high strength and stiffness preventing the particle movement during vibration. The rising

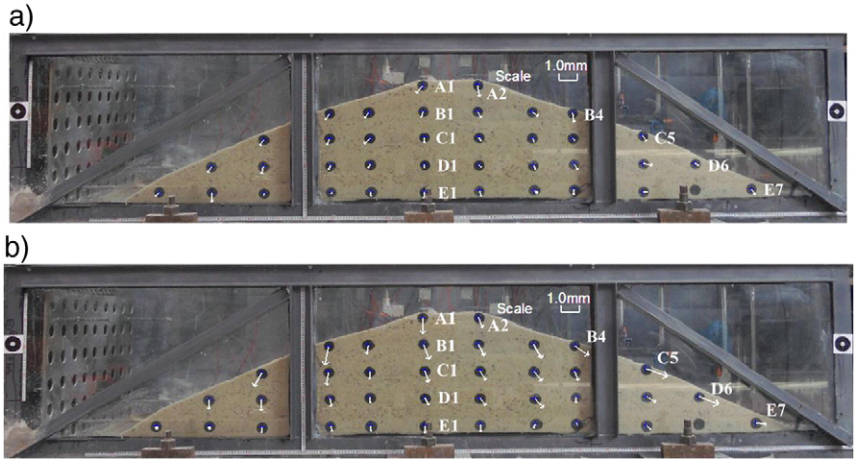

Fig. 11. The displacements of the trace points in Dam II with different seismic waves in: (a) Step 24 (*X*-directional); (b) Step 27 (*X*- and *Z*-directional).

Fig. 12. The displacements of the trace points in Dam II with different PGAs in: (a) Step 31 (PGA = 0.071 g); (b) Step 38 (PGA = 0.2 g); (d) Step 45 (PGA = 0.41 g).

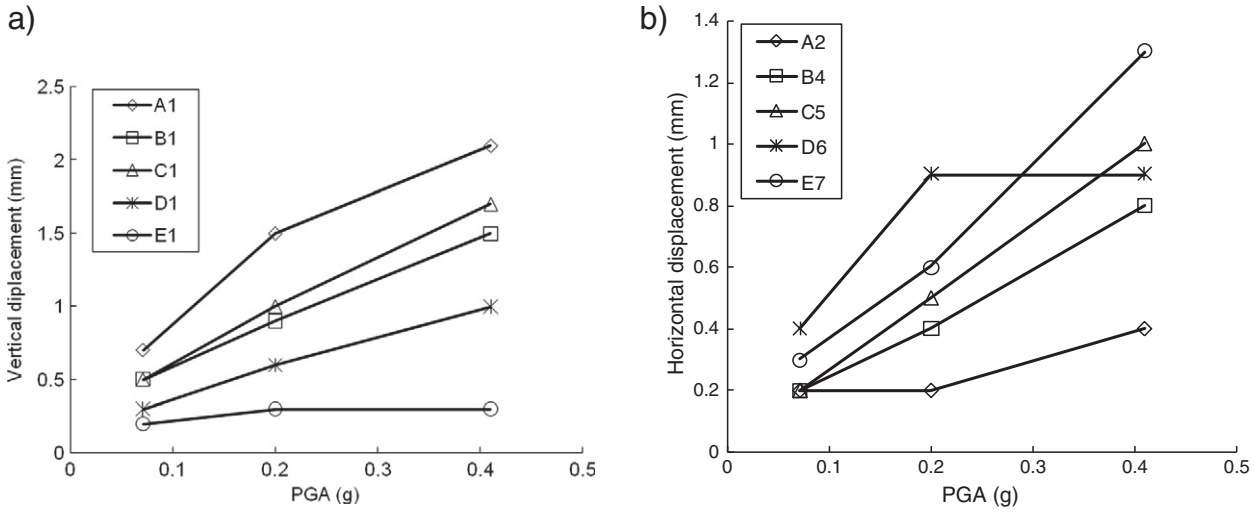

Fig. 13. The displacement of some typical trace points as the PGA: (a) vertical; (b) horizontal.

of water depth largely reduced the suction and incurred larger settlements. The dissipation of water pressure after vibration also caused downward displacements. Besides, seepage occurred during testing, which might wash out some fine dam materials and cause the settlements of the dam (Chang and Zhang, 2011; Chang et al., 2013). As shown in Fig. 15, the seepage water volume in Dam II was larger than that in Dam I, but only the materials in Dam I was washed out because of more fine particles.

5.2.4. Dam materials

Table 9 shows the comparison of the displacement of some typical trace points of the two kinds of dam materials in the test case Step 24. It is found that the deformations of Dam I were larger than those in Dam II. The maximal difference in vertical displacement was 2.7 mm and that in horizontal displacement was 1.3 mm. This can also be

Table 8
The displacements of the typical trace points in Dam II in Step 17 (water depth = 0 m) and Step 45 (water depth = 0.25 m).

Displacement direction	Trace points (shown in Figure 14)	Displacements (mm)		Difference (mm)
		In Step 17[a]	In Step 45[a]	
Vertical	A1	0.2	2.1	1.9
	B1	0.1	1.5	1.4
	C1	0.2	1.7	1.6
	D1	0.1	1	0.9
	E1	0.2	0.3	0.1
Horizontal	A2	0.1	0.4	0.3
	B4	0	0.8	0.8
	C5	0.1	1.5	1.4
	D6	0.1	0.9	0.8
	E7	0	1.3	1.2

Note:
[a] The seismic wave and water depth are shown in Table 6.

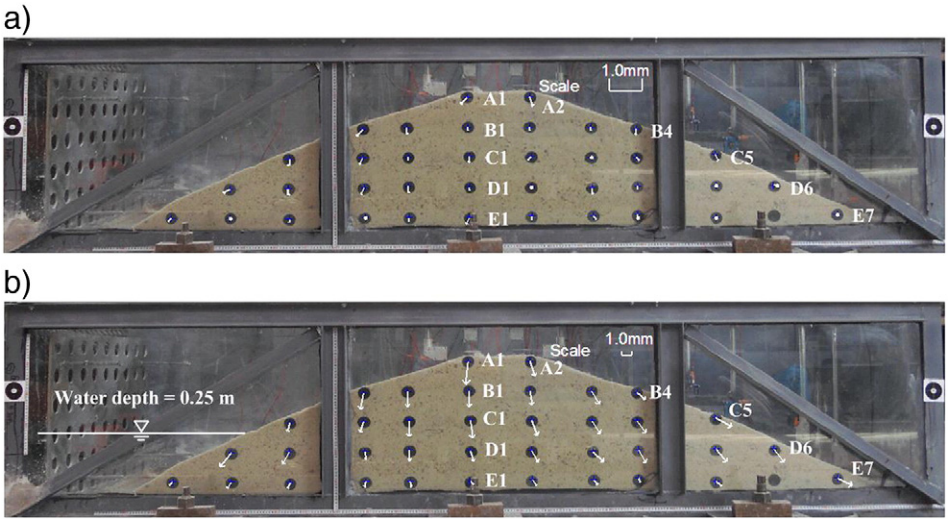

Fig. 14. The displacements of the trace points in Dam II with different water depths in: (a) Step 17 with water depth of 0 m; (b) Step 45 with water depth of 0.25 m.

observed by comparing the values in Dam I (Figure 8) and in Dam II (Figure 11a). Dam I was composed of more fine soil particles (10% kaolin) and there were no particles with the size smaller than 0.1 mm in Dam II, as shown in Fig. 3. Under seismic actions, the vibratory compaction of Dam I was more sufficient than that of Dam II, as more fine particles could move into the pore of coarse particles.

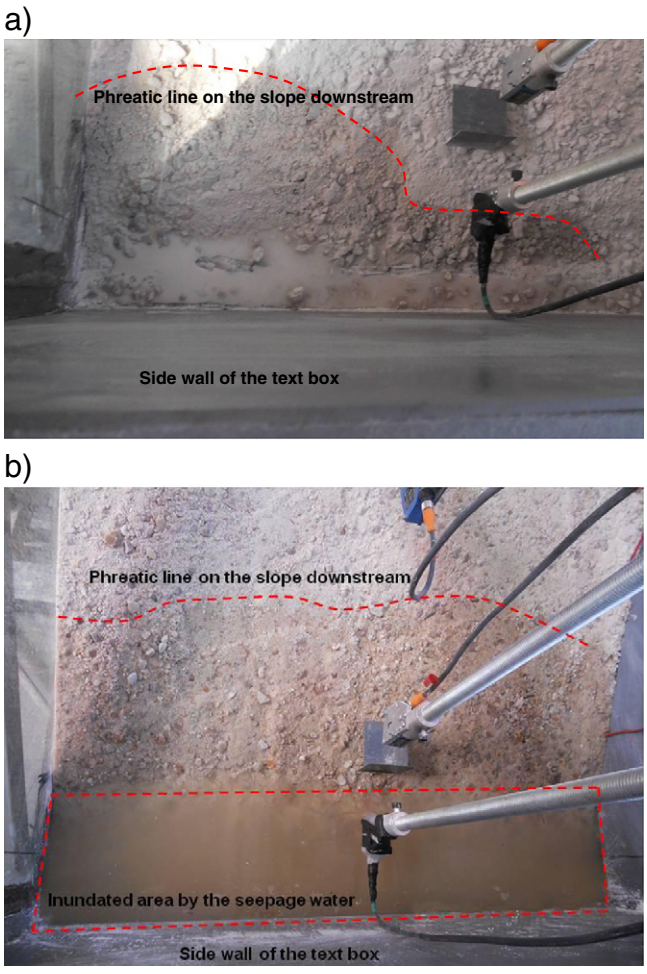

Fig. 15. Seepage at the dam toe downstream (overhead view of the downstream slope toe): (a) In Dam I; (b) In Dam II.

5.3. Discussion and further study

5.3.1. Discussion

(1) The maximum deformation occurs on the surfaces of landslide dams, either on the dam crest or the dam slope. Cracks may be caused by the relatively large deformation, which may quicken the seepage and saturation of the soils. Fig. 16 shows several cracks with the widths of 1 to 2 mm occurred in the upstream slope surface of Dam I.

(2) The coupled influences of seismic actions and water immersion would result in large dam settlements, which may bring forward the dam overtopping failure. Fig. 17 shows the overtopping failure of Dam II after the settlement. Therefore, the landslide dams with high water rising rate under aftershocks should be treated with high priority.

(3) The dams with large content of fine particles had relatively large settlements under seismic actions, as the fine particles are easily to move into the pores of the coarse particles. The overflow time, which is an important index for dam breaching risk analysis, should be estimated by considering the settlements.

Table 9
The displacements of the typical trace points in Dam I and II in Step 24[a].

Displacement direction	Trace points	Displacements (mm)		Difference (mm)
		Dam I	Dam II	
Vertical	A1	3.1	0.4	2.7
	B1	2.9	0.3	2.6
	C1	2.1	0.3	1.8
	D1	1.4	0.2	1.2
	E1	0.6	0.3	0.3
Horizontal	A2	1.5	0.2	1.3
	B3	1.5	0.7	0.8
	D6	1.2	1	0.2
	E7	0.3	0.5	−0.2

Note:
[a] The seismic wave and water depth are shown in Table 6.

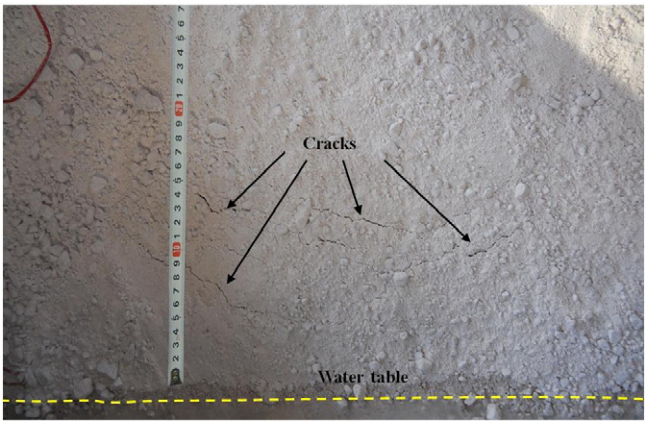

Fig. 16. Cracks on the dam slope surface upstream during water level rising (Dam I).

5.3.2. Further studies

(1) The sampling frequency of the cameras (60 Hz) was not sufficient to measure the real-time acceleration under seismic actions with the frequency as large as 4.7–28 Hz. This may be solved by employing higher speed camera in further studies.
(2) The small-scale model dam is inherently dominated by unsaturated behavior. The magnitude of the capillary stress is out of proportion with the self-weight stress. The quantitative relationship of the model scale and the unsaturated soil effect needs to be further studied.
(3) The soil properties should have been largely changed by the seismic actions, which would influence the stability, failure mode and breach process of the landslide dams. Thus, the soil properties need to be tested and the comparison of the soil properties and the dam breach process with and without seismic actions need to be analyzed.

6. Conclusions

Large scale shaking table tests were conducted to study the dynamic deformation of landslide dams under aftershocks. The videogrammetric technique was employed to measure the deformation and acceleration of the model dams. The following conclusions are drawn:

(1) Seismic actions resulted in settlements and horizontal deformation in landslide dams. The settlements increased from the dam bottom to the dam crest. The displacements of the trace points close to the slope surface of the dam were larger than that of the points in the interior.
(2) Higher peak ground acceleration (PGA) resulted in larger dam deformations due to higher seismic force. The deformations under the combination of *X*- and *Z*-directional shakings were larger than those under *X*-directional shaking due to sufficient vibratory compaction. Water rising led to the increase of dam

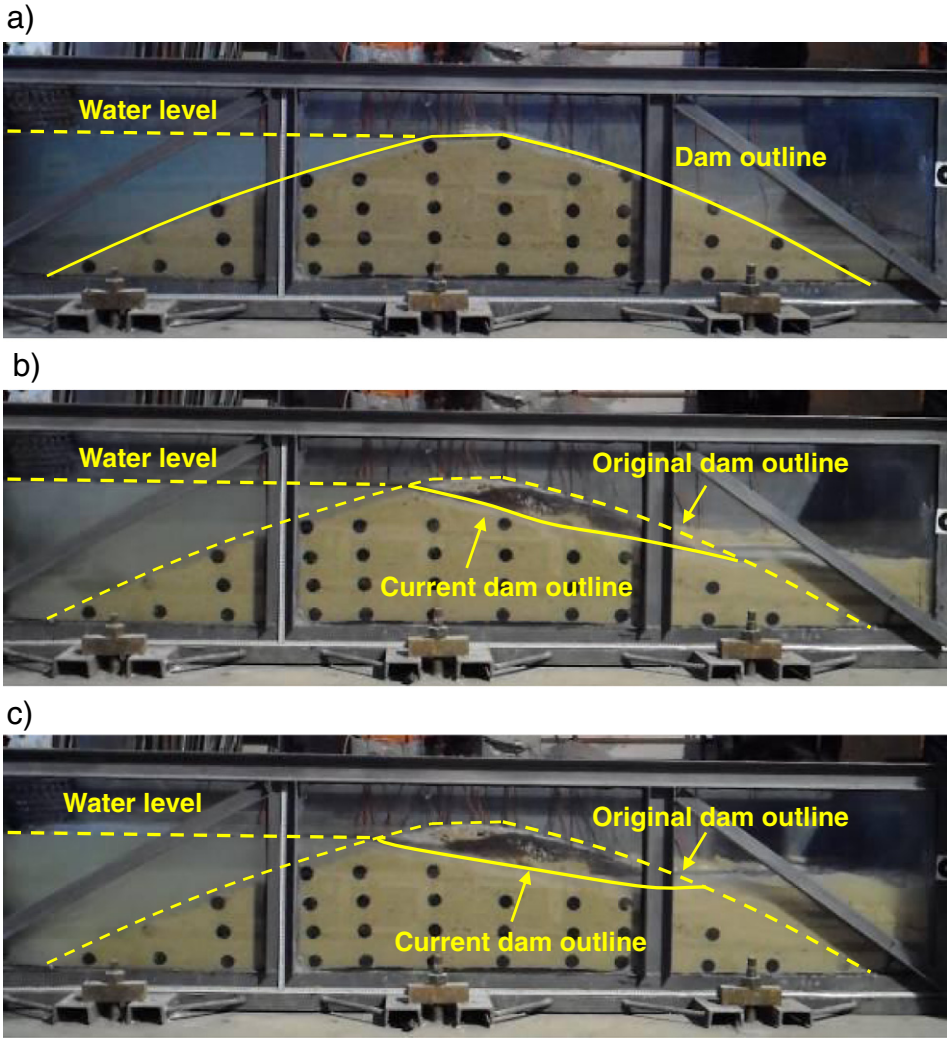

Fig. 17. Breach process of the Dam II: (a) before breaching; (a) during breaching; (c) after breaching.

deformations because that the water seepage reduced the effective soil stress, especially reduced the matric suction. The settlements of the dam composed of more fine particles were larger than that composed of large particle size because that the soil pores in the former were filled more sufficiently with fine particles.

(3) Earthquakes may not lead to dam failure directly, but the cracks and settlements caused by the aftershocks may accelerate the dam failure, normally with overtopping. The coupled influences of seismic actions and water immersion resulted in large dam settlements. Therefore, the landslide dams with high water rising rate under aftershocks should be treated with high priority.

(4) Videogrammetric technique offers multi-metering and dynamic monitoring with relatively high precision and makes no changes on the mechanics properties of the model. The measurement of the dam deformation with this method was good. But the sampling frequency of the cameras (60 Hz) in this study was not sufficient to measure the acceleration under seismic actions with the frequency as large as 4.7–28 Hz. This may be solved by employing higher speed camera in further studies.

Acknowledgments

The research reported in this paper was substantially supported by the National Natural Science Foundation of China (Nos. 41372272 and 41402257), the Shanghai Pujiang Program (14PJ1408200), and the Program for Young Excellent Talents in Tongji University.

References

Burner, A.W., Liu, T.S., 2001. Videogrammetric model deformation measurement technique. J. Aircr. 38 (4), 745–754.
Chang, C.C., Ji, Y.F., 2007. Flexible videogrammetric technique for three-dimensional structural vibration measurement. J. Eng. Mech. 133 (6), 656–664.
Chang, C.C., Xiao, X.H., 2010. Three-dimensional structural translation and rotation measurement using monocular videogrammetry. J. Eng. Mech. 136 (7), 840–848.
Chang, D.S., Zhang, L.M., 2011. A stress-controlled erosion apparatus for studying internal erosion in soils. Geotech. Test. J. 34 (6), 579–589.
Chang, D.S., Zhang, L.M., 2013. Extended internal stability criteria for soils under seepage. Soils Found. 53 (8), 569–583.
Chang, D.S., Zhang, L.M., Xu, Y., Huang, R.Q., 2011. Field testing of erodibility of two landslide dams triggered by the 12 May Wenchuan earthquake. Landslides 8 (3), 321–332.
Cleveland, L.J., Wartman, J., 2006. Principles and applications of digital photogrammetry for geotechnical engineering. Site and Geomaterial Characterization (GSP 149),pp. 128–135.
Costa, J.E., Schuster, R.L., 1988. The formation and failure of natural dams. Geol. Soc. Am. Bull. 100 (7), 1054–1068.
Costa, J.E., Schuster, R.L., 1991. Documented historical landslide dams from around the world. U.S. Geol. Surv. Open File Rep. 91–239, 486p.
Courage, W., Vrouwenvelder, T., van Mierlo, T., Schweckendiek, T., 2013. System behaviour in flood risk calculations. Georisk 7 (2), 62–76.
Cui, P., Zhu, Y.Y., Han, Y.S., Chen, X.Q., Zhuang, J.Q., 2009. The 12 May Wenchuan earthquake-induced landslide lakes: distribution and preliminary risk evaluation. Landslides 6 (3), 209–223.
Davies, T.R., Manville, V., Kunz, M., Donadini, L., 2007. Modeling landslide dam break flood magnitudes: case study. J. Hydraul. Eng. 133 (7), 713–720.
Ermini, L., Casagli, N., 2003. Prediction of the behaviour of landslide dams using a geomorphological dimensionless index. Earth Surf. Process. Landf. 28 (1), 31–47.
Fu, G.K., Moosa, A.G., 2002. An optical approach to structural displacement measurement and its application. J. Eng. Mech. 128 (5), 511–520.
Gruen, A., 1997. Fundamentals of videogrammetry — a review. Hum. Mov. Sci. 16 (2–3), 155–187.
Iai, S., 1988. Similitude for shaking table tests on soil-structure-fluid model in 1 g gravitational field. Rep. Port Harb. Res. Inst. Minist. Transp. Jpn. 27 (3), 1–24.
Ji, Y.F., 2007. Videogrammertic Technique for Structural Dynamic Applications. A PhD dissertation of the Hong Kong University of Science and Technology.
Jongejan, R.B., Calle, E.O.F., 2013. Calibrating semi-probabilistic safety assessments rules for flood defences. Georisk 7 (2), 88–98.
Korup, O., 2002. Recent research on landslide dams — a literature review with special attention to New Zealand. Prog. Phys. Geogr. 26 (2), 206–235.
Liu, X.S., Wang, Z.N., Wang, X.G., Zhao, J.M., Liu, Q.W., 2005. Large-scale Table Model Tests and Dynamic Analysis of CFRD. China Water Power Press, Beijing, pp. 19–41 (in Chinese).
Paikowsky, S.G., Xi, F., 2000. Particle motion tracking utilizing a high-resolution digital CCD camera. ASTM Geotech. Test. J. 23 (1), 123–134.
Peng, M., Zhang, L.M., 2012. Breaching parameters of landslide dams. Landslides 9 (1), 13–31.
Robson, R., Cooper, M.A.R., Taylor, R.N., 1998. A digital imaging system for determining 3D surface displacement in geotechnical centrifuge models. Proceedings of Experimental Mechanics. Balkema, Rotterdam, pp. 647–652.
Shen, W.H., Liu, B.Y., Shi, B.P., 2013. Triggering mechanism of aftershocks triggered by Wenchuan M_w 7.9 earthquake. Acta Seismol. Sin. 35 (4), 461–476 (in Chinese).
Shi, Z.M., Wang, Y.Q., Chen, J.F., Shang, Z.G., He, X.T., 2011. Effect of fill size on the stability of barrier dams. Appl. Mech. Mater. 90–93, 1373–1382.
Shi, Z.M., Wang, Y.Q., Peng, M., Liu, S., 2014. Large scale shaking table tests on dynamic characteristics of landslide dams. Chin. J. Rock Mech. Eng. 33 (4), 707–719 (in Chinese).
Taylor, R.N., Grant, R.J., Robson, S., Kuwano, J., 1998. An image analysis system for determining plane and 3-D displacements in soil models. Proceedings of Centrifuge 98. Balkema, Rotterdam, pp. 73–78.
Xie, P., 2009. Smoothed Particle Hydrodynamics (SPH) Method in Simulating Landslide Movement Process Caused by Strong Earthquakes (M.S. Thesis). Tongji University, Shanghai (in Chinese).
Ye, J., Fu, G.K., Poudel, U.P., 2011. Edge-based close-range digital photogrammetry for structural deformation measurement. J. Eng. Mech. 137 (7), 475–483.
Yu, Q.F., Shang, Y., 2008. Introduction and prospect of videometrics. Sci. Technol. Rev. 26 (24), 84–88 (in Chinese).
Zhang, L.M., Xu, Y., Liu, Y., Peng, M., 2013. Assessment of levee breaching risks to the Pearl River Delta. Georisk 7 (2), 122–133.